BBA - Molecular Basis of Disease 1867 (2021) 166062

Contents lists available at ScienceDirect

BBA - Molecular Basis of Disease

journal homepage: www.elsevier.com/locate/bbadis

Stimulation of cholesterol biosynthesis in mitochondrial complex I-deficiency lowers reductive stress and improves motor function and survival in mice

Tom J.J. Schirris [a,b,1], Sergio Rossell [b,c,1,2], Ria de Haas [b,d,3], Sanne J.C.M. Frambach [a,b,4], Charlotte A. Hoogstraten [a,b], G. Herma Renkema [b,d,5], Julien D. Beyrath [a,b,5], Peter H.G. M. Willems [b,e], Martijn A. Huynen [b,c], Jan A.M. Smeitink [b,d,5], Frans G.M. Russel [a,b,*,6], Richard A. Notebaart [b,c,f,**,6]

[a] Department of Pharmacology and Toxicology, Radboud Institute for Molecular Life Sciences, Radboud University Medical Center, 6500HB Nijmegen, the Netherlands
[b] Radboud Center for Mitochondrial Medicine, Radboud University Medical Center, 6500HB Nijmegen, the Netherlands
[c] Center for Molecular and Biomolecular Informatics, Radboud University Medical Center, 6500HB Nijmegen, the Netherlands
[d] Department of Pediatrics, Radboud University Medical Center, 6500HB Nijmegen, the Netherlands
[e] Department of Biochemistry, Radboud University Medical Center, 6500HB Nijmegen, the Netherlands
[f] Food Microbiology, Wageningen University & Research, 6708WG Wageningen, the Netherlands

ARTICLE INFO

Keywords:
Complex I deficiency
Leigh syndrome
Metabolic network modeling
Cholesterol biosynthesis
NAD(P)H
Ndufs4$^{-/-}$ mice

ABSTRACT

The majority of cellular energy is produced by the mitochondrial oxidative phosphorylation (OXPHOS) system. Failure of the first OXPHOS enzyme complex, NADH:ubiquinone oxidoreductase or complex I (CI), is associated with multiple signs and symptoms presenting at variable ages of onset. There is no approved drug treatment yet to slow or reverse the progression of CI-deficient disorders. Here, we present a comprehensive human metabolic network model of genetically characterized CI-deficient patient-derived fibroblasts. Model calculations predicted that increased cholesterol production, export, and utilization can counterbalance the surplus of reducing equivalents in patient-derived fibroblasts, as these pathways consume considerable amounts of NAD(P)H. We show that fibrates attenuated increased NAD(P)H levels and improved CI-deficient fibroblast growth by stimulating the production of cholesterol *via* enhancement of its cellular efflux. In CI-deficient (*Ndufs4*$^{-/-}$) mice, fibrate treatment resulted in prolonged survival and improved motor function, which was accompanied by an increased cholesterol efflux from peritoneal macrophages. Our results shine a new light on the use of compensatory biological pathways in mitochondrial dysfunction, which may lead to novel therapeutic interventions for mitochondrial diseases for which currently no cure exists.

Abbreviations: ABCA1, ATP binding cassette A1; ALAT, alanine aminotransferase; apo, apolipoprotein; ASAT, aspartate aminotransferase; ATRA, all-trans retinoic acid; CI, complex I; COX, cytochrome-c-oxidase; DIDS, 4,4′-diisothiocyano-2,2′-stilbenedisulfonic acid; EXAMO, EXploration of Alternative Metabolic Optima; PA, piericidin A; PGC-1α, peroxisome proliferator-activated receptor-gamma coactivator 1α; PPAR-α, peroxisome proliferator-activated receptor α; ROS, reactive oxygen species.

* Correspondence to: F.G.M. Russel, Department of Pharmacology and Toxicology, Radboud University Medical Center, PO Box 9101, 6500 HB Nijmegen, the Netherlands.

** Correspondence to: R.A. Notebaart, Department of Agrotechnology and Food Sciences, Wageningen University, PO box 17, 5700 AA Wageningen, the Netherlands.

E-mail addresses: frans.russel@radboudumc.nl (F.G.M. Russel), richard.notebaart@wur.nl (R.A. Notebaart).

[1] These authors contributed equally to the work.
[2] Present address: Royal DSM B.V., Delft, The Netherlands.
[3] Present address: Spierziekten Nederland, Baarn, The Netherlands.
[4] Present address: Future Diagnostics Solutions B.V., Wijchen, The Netherlands.
[5] Present address: Khondrion BV, Nijmegen, The Netherlands.
[6] These authors contributed equally to the work as senior author.

https://doi.org/10.1016/j.bbadis.2020.166062
Received 27 August 2020; Received in revised form 16 December 2020; Accepted 21 December 2020
Available online 13 January 2021

1. Introduction

ATP, the main cellular energy source, is predominantly produced by the mitochondrial oxidative phosphorylation (OXPHOS) system, which consists of five enzyme complexes and two electron carriers. OXPHOS dysfunction is the primary cause of many inherited mitochondrial disorders and has been associated with more common diseases, including cancer, heart failure and neurodegeneration [1–4]. Complex I (CI) is the most frequently affected OXPHOS complex. A deficient activity of this complex is the underlying cause of many mitochondrial disorders, including Leigh syndrome [5,6]. The often early fatal disease typically manifests within the first two years of life and is characterized by elevated blood and cerebrospinal fluid lactate concentrations. At the cellar level ATP production is reduced and reactive oxygen species (ROS) and NAD(P)H levels are increased [6]. Suitable treatment options remain enigmatic.

The detrimental effect of high NAD(P)H levels on cell growth and respiratory capacity was recently illustrated using various genetically-encoded strategies [7,8,9], and was emphasized by its association with cytosolic ROS production by NADPH oxidases [10,11]. Increased mitochondrial NAD(P)H concentrations in CI-deficient cells are probably due to reduced NADH oxidation. This is supported by the negative correlation between residual CI activity and NAD(P)H autofluorescence found in a large panel of CI-deficient patient fibroblasts [6,12], and the decreased NAD^+ levels that paralleled NADH increase in CI-deficient mouse embryonic fibroblasts [13]. NADH could increase cytosolic NADPH levels through the isocitrate/α-ketoglutarate shuttle (Fig. 1A). More recently, proline biosynthesis demonstrated to act as a compensatory mechanism to decrease mitochondrial redox stress, by attenuation of cellular NADH levels [14]. This gives rise to the concept that the flexible nature of cellular metabolic pathways can compensate for the high NAD(P)H levels in CI deficiency.

Here, we used metabolic network modeling to explore such compensatory pathways. The model predicted potentially novel therapeutic targets to lower elevated cellular NAD(P)H levels by stimulating NADPH-consuming cholesterol biosynthesis *via* enhancement of cholesterol export. *In vitro* and *in vivo* studies revealed that fibrate treatment restored NAD(P)H levels and growth rates in CI-deficient patient-derived fibroblasts, and prolonged survival and improved motor function in CI-deficient mice, respectively. Further studies are warranted to evaluate the clinical potential of our findings as a novel option to ameliorate or reverse CI-deficient disease progression.

2. Materials and methods

2.1. Model pre-processing

In this study we used the constraint-based model of human metabolism by Duarte et al. [15], which comprises 2766 metabolites, 3742 reactions and 1905 genes. We identified 9 pairs of reactions with matching stoichiometries but differing reversibilities, and deleted the irreversible member of these pairs (*cf* [16]). Metabolic models were constrained by mimicking the *in vitro* nutrient condition from which the gene expression profiles were determined (Supplementary Table C.1) To obtain a gapless model, necessary for our EXploration of Alternative Metabolic Optima (EXAMO) [17] analysis, we identified and deleted blocked reactions using Flux Variability Analysis [18]. The resulting gapless model comprised 1379 metabolites, 2128 reactions, and 1415 genes, and was used for all modeling studies. All linear equations were solved using IBM's CPLEX optimization toolbox 12.5.

2.2. EXploration of Alternative Metabolic Optima (EXAMO)

We used EXAMO to predict reactions that are likely to be active in control or patient skin fibroblasts. In addition to a gapless constraint-based metabolic model, EXAMO requires a list of highly and lowly expressed metabolic genes. Both for patient and control fibroblasts of each age- and sex-matched pairs, gene expression data of the CI-deficient patient and control fibroblasts have been published previously [19] (GSE27041). We ranked the genes according to their expression level and classified the top 15% as 'highly expressed' and bottom 15% as 'lowly expressed'. The EXAMO algorithm is described elsewhere [17]. Briefly, using the information on highly and lowly expressed genes and the metabolic model's detailed Boolean gene-to-reaction mapping, EXAMO defines sets of highly and lowly expressed reactions. Next, EXAMO solves and explores the alternative optima of a mixed integer linear program that maximizes agreement between gene expression and metabolic fluxes. More precisely, EXAMO finds flux distributions that maximize the sum of the number of highly expressed reactions carrying flux and the number of lowly expressed reactions that do not carry flux. Counting the number of times that a reaction in question is active in the alternative optimal solutions provides a measure for the likelihood that the reaction is indeed active. Reactions active in all alternative solutions are called 'high-frequency reactions' (HFRs) and are predicted to be active in the condition of interest. Reactions that are inactive in all optimal solutions are called 'zero-frequency reactions' (ZFRs) and are predicted to be inactive in the actual cells. EXAMO yielded 27 ZFRs for C6855 and 27 other ZFRs for P6613. With respect to HFRs, these numbers were 447 and 556 for C6855 and P6613, respectively (Supplementary Tables D.1 and E.1). Essentially the same results were obtained with the patient and control fibroblasts of the other age- and sex-matched pairs.

2.3. Cell culture

Primary skin fibroblasts of healthy subjects and CI-deficient patients were derived from skin biopsies in accordance with the applicable rules concerning the review of research ethics committees (Commissie Mensgebonden Onderzoek Regio Arnhem-Nijmegen). Primary skin fibroblasts were maintained in medium M199 containing 5.5 mM glucose and 25 mM HEPES (Life Technologies), supplemented with 10% (*v/v*) fetal bovine serum (FBS, MP Biomedicals) at 37 °C in a humidified atmosphere of 5% (*v/v*) CO_2. HeLa cells (American Type Culture Collection, CCL-2) were maintained at 37 °C in a humidified atmosphere of 5% (*v/v*) CO_2 in Dulbecco's Modified Eagle's medium (DMEM) containing 25 mM glucose, GlutaMAX™, 1 mM pyruvate (Gibco™ Life Technologies, 31966) supplemented with 10% (*v/v)* FBS. All cells were regularly tested for mycoplasma contamination.

2.4. Staining of cellular cholesterol by Filipin III

Primary skin fibroblasts (1000 cells per chamber) were seeded on 8-chamber glass slides (Nunc™ Lab-Tek™ II Chamber Slide™ System, Thermo Scientific) 24 h prior to exposure. After a 24-hour exposure to gemfibrozil, cells were fixed in 3% (*m/v*) paraformaldehyde and 2% glutaraldehyde (*v/v*) in PBS for 1 h in the dark. Next, cellular cholesterol was stained with Filipin III (5% (*m/v*) in dimethylformamide and PBS, 1:50 (*v/v*), Sigma Aldrich) for 1 h in the dark. Images were obtained

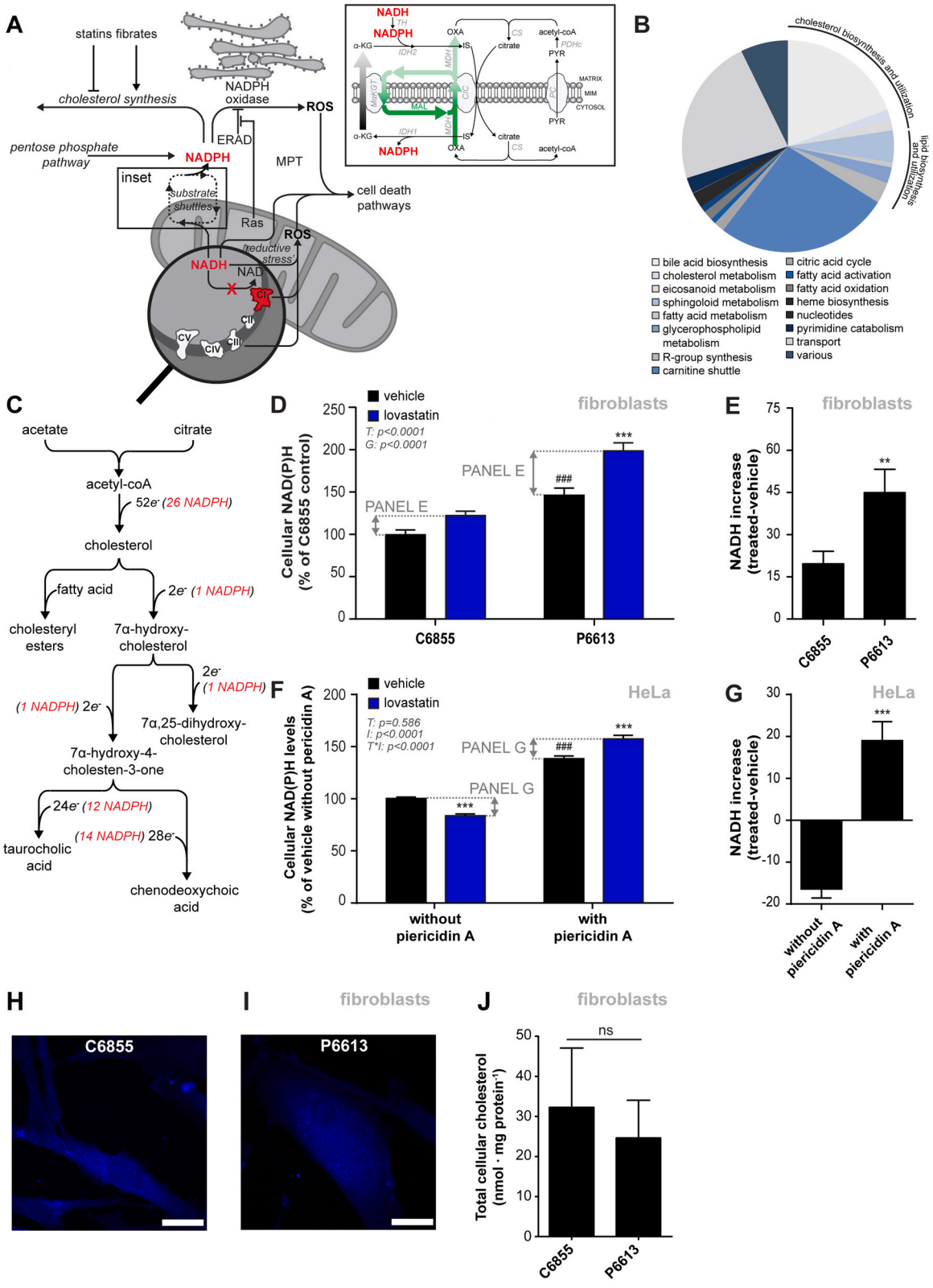

(caption on next page)

Fig. 1. CI-deficient fibroblasts increase cholesterol biosynthesis to compensate for increased cellular NAD(P)H levels. (**A**) Schematic representation of the transfer of reducing equivalents of mitochondrial NADH to cytosolic NADPH, based on the model-predicted involvement of the cytosolic isocitrate dehydrogenase (IDH1) in CI deficiency, and the routes by which increased NADH levels contribute to cell death pathways, including damaging reductive stress and mitochondrial permeability transition (MPT). (**B**) Model-predicted patient-specific metabolic reactions, classified according to Recon1 pathway classes and displayed as a fraction of all patient-specific metabolic reactions. (**C**) Model-predicted reactions of the cholesterol (derivative) biosynthesis pathway using electrons through cytosolic NADPH. (**D**) Cellular NAD(P)H levels were determined after treatment for 24 h with lovastatin hydroxyacid (5 μM) in patient and healthy control fibroblasts ($n \geq 81$ individual cells analyzed in $n = 3$ independent experiments). (**E**) Lovastatin-induced increase in NAD(P)H levels in control and patient fibroblasts. (**F**) NAD(P)H levels were determined after treatment for 48 h with lovastatin hydroxyacid (5 μM) in CI-inhibited (*i.e.* using piericidin A, 1 μM) HeLa cells ($n \geq 160$ individual cells analyzed in $n = 3$ independent experiments). (**G**) Lovastatin-induced changes in NAD(P)H levels in HeLa cells with and without piericidin A-induced CI inhibition. (**H–I**) Filipin III-staining to visualize cellular cholesterol in (**H**) control and (**I**) CI-deficient patient fibroblasts. Scale bars, 50 μm. (**J**) Biochemical determination of cellular cholesterol in these fibroblasts. Data are presented as means ± SEM. (**D, F**) $^{\#\#\#}p < 0.001$ to compare genotype or treatment *vs* vehicle differences or $^{**}p < 0.01$, $^{***}p < 0.001$ to compare treatment effects, by two-way ANOVA (*G*: genotype; *I*: inhibitor (*i.e.* piericidin A); *T*: treatment; *T*I*: treatment*inhibitor interaction) with Bonferroni's *post hoc* analysis. (**E, G, J**). $^{**}p < 0.01$, $^{***}p < 0.001$, ns, not significant, by independent Student's *t*-test.

using an Olympus FV1000 confocal laser scanning microscope (Olympus) equipped with Olympus software FV10-ASW version 1.7.

2.5. Measurement of cellular cholesterol levels

Primary skin fibroblasts ($1.0 \cdot 10^5$ cells) were seeded 24 h prior to determination of cellular cholesterol levels. Cells were harvested and total cholesterol was measured using the Amplex® Red Cholesterol Assay Kit, according to manufacturer's instruction, with the addition of cholesterol esterase, to measure both free and esterified cholesterol (Life Technologies). Cholesterol content was normalized to mg protein in the cell lysate as determined by a Biorad protein assay (Biorad).

2.6. Cholesterol efflux measurements

HeLa cells were seeded (13000 cells·well^{-1}) in DMEM (Sigma Aldrich, D4947) supplemented with 10% (*v/v*) dialyzed FBS. After a 24-hour incubation, the cells were treated with compound in DMEM (Sigma Aldrich, D4947) supplemented with 0.2% (*m/v*) low endotoxin, essentially fatty-acid free bovine serum albumin (BSA). The medium was replaced with DMEM (Sigma Aldrich, D4947) supplemented with 0.2% (*m/v*) BSA containing 1 μCi [^{3}H]-cholesterol and compound in the absence or presence of 1 μM piericidin A (PA). After 24 h of cholesterol loading, the cells were washed twice with medium supplemented with 0.2% (*m/v*) BSA. Subsequently, the medium was replaced with medium supplemented with 0.2% (*m/v*) BSA in the absence or presence of 10 μg·mL^{-1} of the acceptor molecule apolipoprotein (apo) A-I. Resident peritoneal macrophages were isolated by washing the peritoneal cavity twice with 2.5 mL RPMI 1640 medium supplemented with 10 U·mL^{-1} heparin and 2% (*v/v*) FBS. Cells were counted, resuspended, and seeded in 96-well plates at a density of $1.5 \cdot 10^6$ cells·well^{-1}, and incubated at 37 °C in a humidified atmosphere of 5% (*v/v*) CO_2. Four hours after seeding, non-adherent cells were removed. Cholesterol efflux was determined according to a previously described method with slight modifications [20]. After 24-hour incubation, macrophages were loaded with 1 μCi [^{3}H]-cholesterol (Perkin Elmer) in RPMI 1640 medium supplemented with 0.2% (*m/v*) BSA. Next, cells were washed twice with RPMI 1640 medium supplemented with 0.2% (*m/v*) BSA and subsequently cholesterol efflux was allowed to equilibrate for 30 min. The medium was replaced with RPMI 1640 medium supplemented with 0.2% (*m/v*) BSA with or without apoA-I (10 μg·well^{-1}, Merck Millipore). From this step on, the procedure was the same for both cell types. Cholesterol efflux was allowed to proceed for 4 h. Afterwards, we collected the medium and resuspended in scintillant. Cells were lysed by the addition of 0.1% (*m/v*) NaOH for 10 min, and also resuspended in scintillant. Samples were quantified using a scintillation counter (Perkin Elmer Tri Carb 2900TR, Perkin Elmer) and cholesterol efflux was calculated as percentage of radioactivity measured in the medium over total radioactivity (medium plus cells).

2.7. Cholesterol biosynthesis flux analysis

Cholesterol biosynthesis flux in HeLa cells upon lovastatin and gemfibrozil exposure was determined as described previously [21,22]. Briefly, HeLa cells were cultured at a density of 166000 cells·well^{-1} in DMEM (Sigma Aldrich, D4947) supplemented with 10% (*v/v*) dialyzed FBS. After 24 h, cells were washed with serum-free DMEM and incubated with 5 μM lovastatin, 100 μM gemfibrozil or 0.1% (*v/v*) DMSO as vehicle control in serum-free DMEM for 21 h. Cells were exposed to 1 μCi·mL^{-1} ^{14}C-acetic acid sodium salt (Perkin Elmer) with either 5 μM lovastatin, 100 μM gemfibrozil or 0.1% (*v/v*) DMSO as vehicle control for 3 h, followed by washing twice in PBS. Medium and PBS were collected to determine extracellular cholesterol levels. To extract cholesterol lipids, plates were, covered in parafilm, incubated with 1 mL hexane:isopropanol (3:2, *v/v*). After 3 h, medium was collected and evaporated under nitrogen stream. Dried samples were resuspended in chloroform:methanol (3:1, *v/v*), nitrogen-dried and resuspended in 20 μL chloroform:methanol (3:1, *v/v*). 20 μL of medium and cellular samples and 5 mg·mL^{-1} cholesterol standard (Sigma Aldrich) were applied to a TLC silica gel 60 F254 plate (Millipore). Once air-dried, TLC plates were run in 100% chloroform for 20 min and developed with iodine vapor (Iodine beads, Sigma Aldrich). Cholesterol spots were scratched from the plates and mixed with 4 mL Opti-Fluor (Perkin Elmer). ^{14}C-labelled cholesterol was quantified by a liquid scintillation counter (Hidex SL 600, Hidex). Cells were imaged using Leica DM-IL equipped with a 10× objective and manually counted in ImageJ, version 2.0.0-rc-49/1.51d, and used to corrected radioactive counts for cell number.

2.8. Analysis of mitochondrial oxygen consumption

To determine fatty acid-driven mitochondrial oxygen consumption, $1.0 \cdot 10^6$ human skin fibroblasts were resuspended in mitochondrial

respiratory medium (MiR05), before being transferred to the chamber of an Oxygraph-2k (Oroboros) and allowed to reach a stable basal oxygen consumption rate for 10 min. After digitonin permeabilization (10 μg/1 · 10^6 cells, Sigma Aldrich) of the cell membrane, 4 mM butyric acid (Sigma Aldrich), 20 μM palmitoyl-L-carnitine (Sigma Aldrich), and 2 mM malate (Sigma Aldrich) were added to stimulate fatty acid oxidation (STATE4). Finally, maximal ADP-stimulated (STATE3) oxygen consumption was determined by the addition of 4 mM ADP (Sigma Aldrich). Muscle fibers were freshly isolated from *M. quadriceps femoris* as described previously [23], permeabilized by saponin (50 μg·mL^{-1}) treatment at 4 °C for 20 min, and thoroughly washed in respiration medium MiR05. Muscle fiber wet weight was determined and ~8 mg of muscle fibers was transferred to each of the chambers of the Oxygraph-2 k. Palmitoyl-L-carnitine (20 μM, Sigma Aldrich), 4 mM ADP (Sigma Aldrich) and 4 mM malate (Sigma Aldrich) were added to stimulate fatty acid oxidation (STATE4). Finally, maximal ADP-stimulated (STATE3) oxygen consumption was determined by the addition of 4 mM ADP [23,24]. Rotenone (0.5 μM, Sigma Aldrich), and antimycin A (2.5 μM, Sigma Aldrich) were added to inhibit CI and CIII, respectively, and to determine non-mitochondrial respiration. These levels were subtracted from all other respiratory rates. Cytochrome *c* (10 μM, Sigma Aldrich) was added to check the integrity of the mitochondrial outer membrane.

2.9. Measurement of cellular NAD(P)H autofluorescence

For quantitative determination of cellular NAD(P)H autofluorescence, human primary skin fibroblasts (5.0 · 10^4 cells) were seeded in 35 mm Fluorodishes (World Precision Instruments), 24 h prior to compound exposure. After exposure, the medium was replaced by HEPES-Tris (HT) buffer (132 mM NaCl, 4.2 mM KCl, 5.5 mM D-glucose, 1 mM $MgCl_2$, 1 mM $CaCl_2$ and 10 mM HEPES, pH 7.4) and images were obtained using a temperature-controlled chamber attached to a stage of an inverted microscope (Axiovert 200M, Carl Zeiss) equipped with a ×40, 1.25 NA Plan NeoFluar oil immersion objective, as described previously [25]. The cells were excited at 360 nm for 1000 ms using a monochromator (Polychrome IV, TILL Photonics). Fluorescence emission light was directed by a 415DCLP dichroic mirror (Omega Optical Inc.) through a 510WB40 emission filter (Omega Optical Inc.) onto a CoolSNAP HQ monochrome CCD-camera (Roper Scientific). A similar procedure was used for NAD(P)H quantification in HeLa cells. Briefly, HeLa cells were seeded at a density of 10000 cells in DMEM containing 1 g·L^{-1} glucose (Sigma-Aldrich, D4947) supplemented with 10% (*v/v*) dialyzed FBS and incubated overnight. Next, the compounds were added as described above. After 24 h, the medium was replaced with medium containing compounds in the presence or absence of 1 μM piericidin A. After another 24-hour incubation, medium was replaced by HT buffer for image acquisition. Images were recorded as described above for the human primary skin fibroblasts. After background subtraction, average cellular intensity was determined using Image Pro Plus 6.0.0.260 software (Media Cybernetics) to determine NAD(P)H levels.

2.10. Catalytic capacity of individual OXPHOS complexes

Primary skin fibroblast pellets were snap frozen in liquid nitrogen, and kept at −80 °C until use. Cell pellets were resuspended in 10 mM Tris-HCl and pottered, followed by the addition of sucrose (215 mM). The lysate was cleared of unbroken cells by centrifugation (10 min, 600*g*), after which the supernatant containing mitochondria was pelleted at 14000*g* for 10 min, resuspended in 10 mM Tris-HCl (pH 7.6) and snap frozen in aliquots. Catalytic capacity of OXPHOS complexes was measured spectrophotometrically in duplicate, as described previously [26]. Briefly, the following substrates were used: NADH (0.2 mM, Roche) and coenzyme Q_1 (70 μM, Sigma Aldrich) for CI; succinate (10 mM, Sigma Aldrich) and decylubiquinone (80 μM, Enzo Life Sciences) for CII; decylubiquinol (300 μM, Enzo Life Sciences) and cytochrome *c* (50 μM, Sigma Aldrich) for CIII; reduced cytochrome *c* (70 μM, Sigma Aldrich) for CIV; and ATP (3 mM, Sigma Aldrich) for CV. For the determination of the ATPase activity of CV, 10 μM oligomycin was used to correct for non-CV ATPase activity. CI-CV values were normalized to the activity of the mitochondrial matrix enzyme, citrate synthase, to correct for differences in mitochondrial mass. Citrate synthase was determined spectrophotometrically in duplicate as described before [26].

2.11. Analysis of mitochondrial area

Human skin fibroblasts (5.0 · 10^4 cells) were seeded in 35 mm Fluorodishes (World Precision Instruments), 24 h prior to gemfibrozil (100 μM) exposure. To determine the mitochondrial area, cells were loaded with 100 nM tetramethylrhodamine methyl ester (TMRM) for 25 min at 37 °C, as described previously [27]. Subsequently, images were obtained using a temperature-controlled chamber attached to a stage of an inverted microscope (Axiovert 200 M, Carl Zeiss) equipped with a ×63, 1.25 NA Plan NeoFluar oil immersion objective. Cells were maintained in HT buffer for image acquisition. Image analysis consisted of subtraction of background intensity, after which images were masked with a binarized image for mitochondrial morphology using Image Pro Plus 6.3 software (Media Cybernetics).

2.12. Growth curve construction

Twenty-four hours prior to gemfibrozil exposure, primary skin fibroblasts were seeded in 96-wells black/clear imaging plates (Santa Cruz Biotechnology) at a density of 1000 cells/well in DMEM medium supplemented with 10% (*v/v*) FBS). A 1000× concentrated serial $\sqrt{10}$-dilution of gemfibrozil was made in DMSO. Immediately before use, this gemfibrozil stock solution was diluted 100× in PBS, and 10× in culture medium, resulting in a final DMSO concentration of 0.1% (*v/v*). Three replicates of each concentration were tested up to a maximum concentration of 100 μM. After 24-hour exposure, nuclei were stained using Hoechst 33342 (20 μg·mL^{-1}, Life Technologies) for 20 min at 37 °C. Fluorescence was imaged on a BD Pathway 855 high-throughput microscope (Becton Dickinson (BD) Bioscience). The number of nuclei per image was analyzed using CellProfiler [28]. Linear regression analysis of the natural log-transformed exponential part of the growth curves was performed and the doubling time was calculated from the inverse slope of the linear fit.

2.13. Mice

Initial breeding pairs of heterozygous *Ndufs4*$^{+/-}$ mice (mixed 129/Sv: C57BL6 background) [29,30] were kindly provided by the Palmiter

laboratory (University of Washington, Seattle) and sustained in our (specific pathogen free) breeding facility. *Ndufs4*$^{+/-}$ mice were intercrossed to produce *Ndufs4*$^{-/-}$ mice. All mice were group-housed under controlled conditions (temperature 20–22 °C, humidity 50–70%) with free access to standard food (V1534–300 R/M-H from Ssniff GmbH, Soest, Germany)) and water and maintained on a 12-hour light/dark cycle (lights on at 7 am), as described previously [31]. Pups received toe tattoos for identification and tail clips were taken for genotyping at PD 8. Then wildtype and *Ndufs4*$^{-/-}$ mice were assigned to each treatment group using manual randomization. Randomization of housing conditions was performed by manual randomization of the cage location within the animal room (rack/shelf). Administration of treatments and result assessment were performed blinded. Sample sizes and power calculations were bases on previous studies using the *Ndufs4*$^{-/-}$ mice by ourselves and others [31,32]. Experiments part of this study (incl. sampling, outcome assessment, analysis) were performed blinded. Animal caretakers and researchers were also blinded during day-to-day animal care concerning treatment group. Both female and male *Ndufs4*$^{-/-}$ and wildtype mice were treated *via* intraperitoneal injection with 100 mg·kg bodyweight^{-1}·day^{-1} fenofibric acid ($n = 8$ wildtype, $n = 8$ *Ndufs4*$^{-/-}$, Sigma Aldrich) or vehicle ($n = 13$ wildtype, $n = 10$ *Ndufs4*$^{-/-}$, 0.9% (*m/v*) NaCl solution), from PD 20 onwards. All mice were weaned at the age of postnatal day (PD) 24. *Ndufs4*$^{-/-}$ mice were always housed with a minimum of one wildtype littermate for warmth and provided with food on the bottom of the cage. Mice were weighed daily and clinical symptoms were observed. Based on ethical considerations and regulations it should be stated that no permission was obtained to pass the so-called humane endpoint, indicated by the severity of clinical symptoms observed in combination with a body weight loss of >20%. Ethical approval was obtained by the Committee for Animal Care and Experimental Use of the Radboud University Medical Center Nijmegen, The Netherlands (ref. no. 2013-210 and 2017-0017). Experiments were carried out in agreement with the Dutch laws, ARRIVE guidelines and the European Communities Council Directive (2010/63/EU).

2.14. Motor function assessment

Motor function was assessed using the CatWalk system (Noldus), which is an automated gait analysis system to objectively assess motor function in rodents and previously used for the *Ndufs4*$^{-/-}$ mice [31,32]. At PD 27 and PD 28, mice were habituated to the CatWalk with their cage mates for 10 min. Testing was performed individually in the dark, starting at PD 30. A walking session was successful after completing three compliant runs. A compliant run meets the run criteria set at a maximum run duration of 10 s.

2.15. ALAT and ASAT determination

Plasma alanine aminotransferase (ALAT) and aspartate aminotransferase (ASAT) levels were determined biochemically, as previously described [33]. Briefly, the samples were diluted 1:20 in either ALAT reaction solution (100 mM tris(hydroxymethyl)aminomethane, 500 mM L-alanine, 0.18 mM NADH, 0.1 mM pyridoxal-5′- phosphate, 1700 U·L^{-1} lactate dehydrogenase, pH 7.15) or ASAT reaction solution (80 mM tris(hydroxymethyl)aminomethane, 240 mM L-aspartate, 0.18 mM NADH, 0.1 mM pyridoxal-5′- phosphate, 600 U·L^{-1} malate dehydrogenase, 900 U·L^{-1} lactate dehydrogenase, pH 7.65). To start the ALAT or ASAT measurements, 15 mM or 12 mM 2-oxoglutaric acid was added to the sample, respectively. Finally, the absorbance at 340 nm was measured using a Biorad Benchmark Plus spectrophotometer for 10 min at 37 °C (Biorad Laboratories). The enzyme activity was derived from the linear range of the curve.

2.16. Hepatic lipid quantification

Liver samples (25 mg) were resuspended in 1 mL ice-cold isopropanol (Merck) to isolate lipids. The liver samples were homogenized by tissue grinding and sonication for 20 min in ice water. After centrifugation, the supernatant containing the lipids was evaporated at 65 °C. The residual lipid pellet was resuspended in isopropanol and stored at −20 °C until quantification. Lipid quantification was performed by spectrophotometric sulfo-phospho-vanillin assessment as previously described, with minor modifications [34]. Briefly, samples were diluted 1:1 in isopropanol and incubated at 90 °C for 30 min to evaporate all organic solvents. The pellets were resuspended in 95% (*m/v*) sulphuric acid (Merck) and incubated at 90 °C for 20 min. Next, the samples were rapidly cooled for 5 min at 4 °C. Pre-vanillin absorbance levels were determined using a Biorad Benchmark Plus spectrophotometer at 535 nm (A_{535}). Then, 0.2 mg·mL^{-1} vanillin (Sigma Aldrich) in 17% (*v/v*) aqueous phosphoric acid (Merck) was added to the samples (1:2 ratio). After a 10-minute light protected incubation at room temperature, post-vanillin absorbance levels were determined (A_{535}). Lipid levels were defined as the difference between pre-vanillin and post-vanillin absorbance levels. Vehicle-treated wildtype mice were set at 100% to compare lipid levels in liver samples.

2.17. Histology

Livers were dissected and post-fixed overnight with 4% (*v/v*) formaldehyde, and subsequently embedded in paraffin. Liver slices of 5 μm were obtained and stained with Mayer's hematoxylin for 3 min. Subsequently, sections were washed (water 5 min, 1% (*m/v*) $NaHCO_3$ 1 min, water, ethanol) and counterstained with 0.25% (*v/v*) eosin Y for 30 s. Finally, the slices were dehydrated using a series of alcohol solutions and mounted. Images were acquired using a Panoramic 250 Flash III digital slide scanner (3DHistech Ltd.) and analyzed using Panoramic Viewer software (3DHistech Ltd.).

2.18. Statistical analysis

Curve-fitting and statistical analysis was performed using GraphPad Prism 5.03 software (GraphPad Software Inc.) and SPSS statistics 22 (IBM). Unless indicated otherwise, all results are presented as mean ± SEM. Survival curves were analyzed by log-rank Mantel-Cox analysis. Body weight was compared using linear mixed model analysis. Differences between groups were tested with one- or two-way ANOVA analysis and appropriate *post hoc* analysis as indicated in the figure legends.

2.19. Key resources table

Reagent or resource	Source	Identifier
Chemicals, peptides, and recombinant proteins		
^{14}C-acetic acid sodium salt	Perkin Elmer	Cat # NEC08H
Adenosine diphosphate sodium salt	Sigma Aldrich	Cat # A2754
Adenosine triphosphate magnesium salt	Sigma Aldrich	Cat # A9187
All-trans retinoic acid	Sigma Aldrich	Cat # R2625
Antimycin A	Sigma Aldrich	Cat # A8674
Apolipoprotein A-I	Merck Millipore	Cat # 178452
Bezafibrate	Sigma Aldrich	Cat # B7273
Calcium chloride	Sigma Aldrich	Cat # 22,350-6
Clofibric acid (referred to as clofibrate)	Sigma Aldrich	Cat # 90323
Cholesterol	Sigma Aldrich	Cat # C8667
Coenzyme Q_1	Sigma Aldrich	Cat # C7956
Cytochrome c	Sigma Aldrich	Cat # C2506
4,4′-Diisothiocyanotostilbene-2,2′-disulfonic acid	Sigma Aldrich	Cat # D3514
Decylubiquinone	Enzo Life Sciences	Cat # BML-CM115
D-Glucose	Sigma-Aldrich	Cat # G7021
Dimethylformamide	Merck	Cat # 28.02.02
Fenofibrate	Sigma Aldrich	Cat # 49562-28-9
Filipin III	Sigma Aldrich	Cat # F4767
Gemfibrozil	Sigma Aldrich	Cat # G9518
GW6471	Cayman Chemical Company	Cat # 11697
HEPES	Sigma Aldrich	Cat # H3375
Heparin sodium salt	Sigma Aldrich	Cat # H3393
Hoechst 33342	Thermo Fisher Scientific	Cat # H1399
[1,2-^{3}H(N)]-cholesterol	Perkin Elmer	Cat # NET139
Lactate dehydrogenase	Roche	Cat # 10127230001
L-Alanine	Sigma Aldrich	Cat # 05129
L-Aspartic acid sodium salt	Sigma Aldrich	Cat # A6683
Lovastatin hydroxyacid sodium salt	Toronto Research Chemicals Inc.	Cat # L472250
Magnesium chloride	Merck	Cat # 1.05833.0250
L-Malic acid	Sigma Aldrich	Cat # M1000
NADH	Roche	Cat # 10107735001
Oligomycin	Sigma Aldrich	Cat # O4876
2-Oxoglutaric acid	Sigma Aldrich	Cat # K3752
Palmitoyl-L-carnitine	Sigma Aldrich	Cat # 61251
Piericidin A	Santa Cruz Biotechnology	Cat # SC-202287
Pyridoxal-5′-phosphate	Sigma Aldrich	Cat # P9255
Potassium chloride	Merck	Cat # 1.04936.1000
Rotenone	Sigma Aldrich	Cat # R8875
Sodium butyrate	Sigma Aldrich	Cat # 10,341-0
Sodium chloride	Sigma Aldrich	Cat # 31434
Sodium succinate	Sigma Aldrich	Cat # S2378
Sulphuric acid	Merck	Cat # 1.00731.1000
Tetramethylrhodamine methyl ester	Thermo Fisher Scientific	Cat # T668
TO-901317	Sigma Aldrich	Cat # 575310
Tris(hydroxymethyl)aminomethane	Thermo Fisher Scientific	Cat # 15504-020
Vanillin	Sigma Aldrich	Cat # V1104
Critical commercial assays		
Amplex® Red cholesterol assay kit	Life Technologies	Cat # A12216
Experimental models: organisms/strains		
Primary cells: Healthy control-derived skin fibroblasts	Radboud Center for Mitochondrial Medicine Biobank	N/A
Primary cells: CI-deficient patient-derived skin fibroblasts	Radboud Center for Mitochondrial Medicine Biobank	N/A
Mice: *Ndufs4*$^{-/-}$(*Ndufs4*$^{tm1.1Rpa}$)	Dr. Richard Palmiter	N/A

3. Results

3.1. Increased cholesterol biogenesis in CI-deficient fibroblasts associates with cellular NAD(P)H levels

CI-deficient patient and control-specific metabolic models were constructed using the EXAMO algorithm [17] by integrating previously generated gene expression data of primary skin fibroblasts of five patients and their age- and sex-matched controls [19] (Supplementary Table A.1). Comparison of these models resulted in 126 reactions predicted to be exclusively active in patient fibroblasts and, therefore, expected to have largest relevance to the disease state (Supplementary Table B.1, Fig. 1B). Next, we selected these pathways which consume most electrons and consequently are expected to most effectively reduce harmful cellular NAD(PH) levels. This resulted in 14 pathways involved in lipogenesis and 28 in the biosynthesis of cholesterol and its derivatives (Fig. 1B–C).

Although both pathways consume considerable amounts of NADPH, lipogenesis utilizes more ATP. Considering the reduced ability to produce ATP in a CI-deficient condition the cholesterol biosynthesis is more likely to correct the high NAD(P)H levels, as compared to lipogenesis. In line with a compensatory role for the cholesterol biosynthesis,

utilization (*e.g.* bile acid and sterol biosynthesis) and efflux expression of various genes of these pathways was increased CI-deficient patients compared to healthy controls (Supplementary Fig. A.1A–C). Next, we further explored whether this could indeed compensate for the disease phenotype by measuring NAD(P)H levels in fibroblasts of the patient with lowest residual CI activity and poorest survival (P6613) and its matched control (C6855) (Supplementary Table A.1), with or without 24-hour treatment with the HMG-CoA reductase (*i.e.* the rate-limiting step of the cholesterol biosynthesis) inhibitor lovastatin. In line with previous observations [6], total cellular NAD(P)H levels were significantly increased in patient fibroblasts (Fig. 1D, Supplementary Fig. A.2A–B). Inhibition of cholesterol biosynthesis by lovastatin resulted in a significantly higher increase of cellular NAD(P)H levels in the patient cells (Fig. 1E), which was not due to an inhibition of OXPHOS

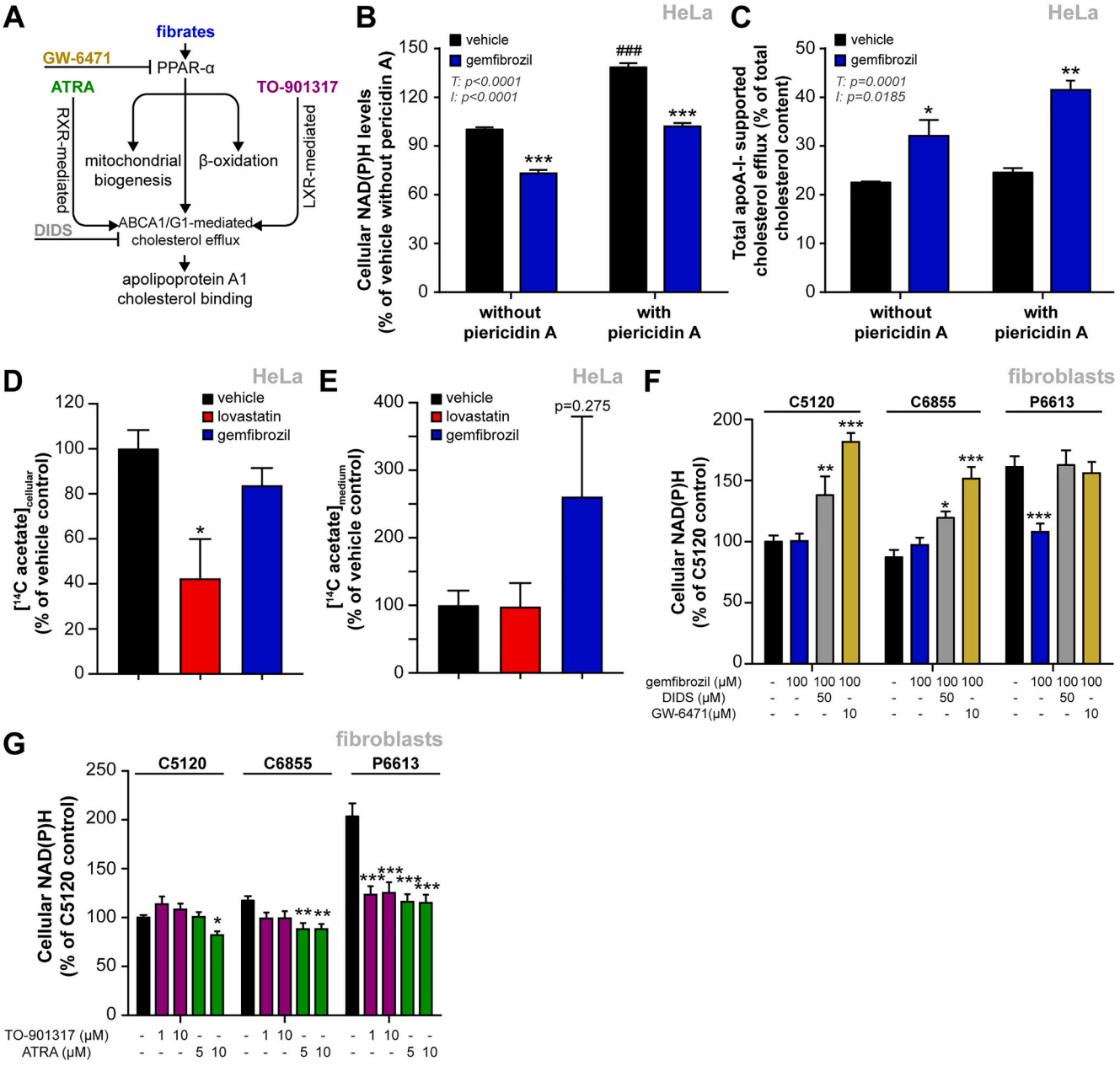

Fig. 2. Fibrate-induced cholesterol efflux and biosynthesis decreases cellular NAD(P)H levels in CI-deficient cells *via* PPAR-α-dependent upregulation of ABCA1. (**A–B**) Cellular NAD(P)H levels were determined after treatment for 48 h with gemfibrozil (100 μM) of CI-inhibited (*i.e.* using piericidin A) HeLa cells ($n \geq 148$ individual cells analyzed in $n = 3$ independent experiments). (C) Apolipoprotein A-I (apoA-I)-supported cellular cholesterol efflux was determined after treatment for 48 h with gemfibrozil (100 μM) of CI-inhibited HeLa cells loaded with [^{3}H]-cholesterol and expressed as the percentage of all radioactively labelled cholesterol (*i.e.* present in both cellular and medium fractions). (D–E) Cellular *de novo* cholesterol synthesis flux was determined by the formation of radiolabeled (^{14}C) cholesterol from ^{14}C-acetate. ^{14}C-cholesterol levels were determined after 24-hour treatment with lovastatin hydroxyacid (■, 5 μM) or gemfibrozil (■, 100 μM) in (D) cellular and (E) extracellular fractions. (F–G) To study the effect of fibrates on NAD(P)H levels, (F) control and patient fibroblasts (normalized to C5120 VEH (93 ± 5 AU) were treated for 24 h with (■) or without (■) gemfibrozil (100 μM, 24-hour) with or without DIDS (■, 50 μM), or GW-6471 (■, 10 μM), and (G) after TO-901317 (■) or all-trans retinoic acid (ATRA, ■); $n \geq 29$ cells in each experiment ($n = 3$). Data are presented as means ± SEM. (B–C) $^{###}p < 0.001$ to compare inhibitor *vs* vehicle differences or $^{*}p < 0.05$; $^{**}p < 0.01$; $^{***}p < 0.001$ to compare treatment effects, by two-way ANOVA (*I*: inhibitor (*i.e.* piericidin A); *T*: treatment; *T*I*: treatment*inhibitor interaction) with Tukey's *post hoc* analysis. (D, E, F, G) $^{*}p < 0.05$; $^{**}p < 0.01$; $^{***}p < 0.001$ to evaluate treatment effects, by one-way ANOVA with Dunnett's (D, E) or Bonferroni's (F, G) *post hoc* analysis.

complex activity (Supplementary Fig. A.3A–B) [24].

To further investigate the relation between cholesterol biosynthesis and cellular NAD(P)H pools we induced CI-deficiency in HeLa cells with piericidin A (PA), as recently described [8]. In accordance with previous studies, we could demonstrate increased total cellular NAD(P)H levels in these cells as a consequence of the reduced NADH oxidation by CI (Fig. 1F, Supplementary Fig. A.2C–D). These levels were elevated to a similar extent as observed in CI-deficient patient fibroblasts (Fig. 1D). Interestingly, lovastatin mildly decreased NAD(P)H levels in control HeLa cells, which may align by previous observations that lovastatin exposure of cancerous cell lines can inhibit their glucose uptake and glycolytic rates [35]. The mild lovastatin-induced reduction in NAD(P)H could be explained by the cytosolic NADH autofluorescence signal that heavily depends on the glycolytic NAD(P)H production [36]. This idea is supported by the absence of such an effect of lovastatin in healthy control fibroblasts, which rely more on oxidative metabolism [37]. Importantly, in PA-treated HeLa cells, inhibition of cholesterol biosynthesis by lovastatin resulted in a significantly higher increase in cellular NAD(P)H, as compared to their untreated counterparts (Fig. 1F–G), which supports the idea that, compared to healthy control cells, CI-deficient cells have a greater dependence on cholesterol biosynthesis to maintain NAD(P)H levels.

Although these results substantiate the relevance of cholesterol biosynthesis for patient cells, endogenous stimulation of this pathway, as inferred from the gene expression data in the context of the metabolic model, does not fully compensate the disease phenotype. Furthermore, total cholesterol content of patient cells was not different from control cells (Fig. 1H–J), indicating a tight regulation of cellular cholesterol levels. We therefore explored pharmacological strategies to further enhance cholesterol biosynthesis *via* stimulation of its cellular efflux.

3.2. Pharmacological stimulation of ABCA1-dependent cholesterol efflux decreases cellular NAD(P)H levels and normalizes cellular growth rates

Fibrates stimulate cellular cholesterol extrusion by increasing plasma membrane expression of the ATP-binding cassette subfamily A1 (ABCA1) efflux transporter through activation of peroxisome proliferator-activated receptor alpha (PPAR-α) [38] (Fig. 2A). In line with our hypothesis that increased cholesterol efflux will stimulate NADPH consumption by the cholesterol biosynthesis, cellular NAD(P)H levels in CI-inhibited HeLa cells were normalized to control levels upon 24-hour treatment with gemfibrozil, a fibrate commonly used to treat hypercholesterolemia (Fig. 2B). To investigate whether this effect was accompanied by an increased cellular cholesterol efflux we first loaded cells with radio-labelled cholesterol, after with the apolipoprotein (apo) A-I-supported cellular cholesterol efflux was allowed to occur as described previously [20]. In line with our hypothesis, gemfibrozil increased the cholesterol efflux rates (Fig. 2C), which confirms that gemfibrozil acted *via* ABCA1, as apo A-I specifically interacts with ABCA1 [20]. To investigate whether the increased efflux indeed leads to an increased cholesterol biosynthesis, we determined the *de novo* cholesterol biosynthesis flux (Fig. 2D–E). Treatment of HeLa cells with lovastatin resulted in decreased *de novo* synthesized cellular cholesterol (Fig. 2D). Although the higher cholesterol efflux upon gemfibrozil treatment increases the total extracellular cholesterol concentration, extracellular concentration of newly synthesized cholesterol only tented to be increased, albeit this was not statistically significant. It has to be noted that we observed a low signal-to-noise ratio in this assay, which led to an increased deviation of the experimental data (Fig. 2E). Taken together, the NAD(P)H-lowering effect of gemfibrozil seems to depend on an increased cholesterol efflux and biosynthesis leading to enhanced cellular NADPH consumption.

Gemfibrozil could also reduce the increased cellular NAD(P)H levels in patient fibroblasts (P6613) to control levels upon 24-hour treatment (Fig. 2F), without altering these levels in control (C6855 and C5120) fibroblasts. Interestingly, we observed a decrease in NAD(P)H levels upon treatment with gemfibrozil in control HeLa cells. This difference between cell types may be explained by variations in the metabolic phenotype, where fibroblasts have a more oxidative metabolism [37] and HeLa cells have a more glycolytic phenotype. Therefore, more cytosolic NAD(P)H could have been available for the cholesterol biosynthesis to be used upon stimulation of the efflux by gemfibrozil. Combined with the notion that the cytosolic NAD(P)H autofluorescence signal heavily depends on the glycolytic NADH production [36], this could explain the decreased NAD(P)H levels in control HeLa cells upon gemfibrozil treatment. Inhibition of ABCA1 or PPAR-α, by DIDS and GW-6471 (Fig. 2A), respectively, completely abolished the gemfibrozil-induced decrease in NAD(P)H levels in patient fibroblasts, whereas they increased NAD(P)H levels in control cells (Fig. 2F).

PPAR-α forms heterodimers with the retinoid X (RXR) or the liver X (LXR) receptor, and stimulation of these receptors with all-trans retinoic acid (ATRA) and TO-901317, respectively, virtually normalized the level of NAD(P)H in patient fibroblasts, whereas ATRA slightly but significantly decreased this level in control fibroblasts (Fig. 2G). This confirms the role of PPAR-α and ABCA1 in the mechanism underlying the gemfibrozil-induced normalization of cellular NAD(P)H levels in CI deficiency.

Next, we evaluated the dose-dependent characteristics of the gemfibrozil-induced decrease in NAD(P)H levels in patient fibroblasts (Fig. 3A) and found a maximal normalizing effect around its EC_{50} value for PPAR-α (193 μM; [39]), further supporting the involvement of the PPAR-α/LXR/ABCA1 axis in these effects. To strengthen the role of PPAR-α, we also evaluated three other PPAR-α agonists (*i.e.* clofibrate, fenofibrate, and bezafibrate [39]), which essentially gave the same result (Fig. 3B-D). However, at the highest concentration used, clofibrate and bezafibrate increased NAD(P)H levels in one of the control cells (C6855) (Fig. 3B and D). Similarly to gemfibrozil, a maximal normalizing effect was observed around their EC_{50} values for PPAR-α (*i.e.* clofibrate 55 μM, fenofibrate 30 μM, bezafibrate: 50 μM). Since stimulation of cholesterol biosynthesis lowers reductive stress, it can be expected to beneficially affect overall cell function. Indeed, gemfibrozil ameliorated the impaired growth of patient fibroblast cell line P6613 (Fig. 3E–G) and even more potently of line P7898 (Fig. 3H). On the other hand, no significant effect on cell growth was observed in P6173 and P5866 fibroblasts (Fig. 3I–J). Together, these results support our hypothesis that increasing cholesterol biosynthesis provides a therapeutic target to counteract the deteriorating effects of CI deficiency.

3.3. Cholesterol efflux stimulation increases lifespan and motor function of *Ndufs4*$^{-/-}$ mice accompanied by stimulation of macrophage cholesterol efflux

Subsequently, we investigated whether fibrates could also have a beneficial effect *in vivo* in *Ndufs4*$^{-/-}$ mice (mixed 129/Sv: C57BL6 background), a validated model for CI-deficiency phenotypically mimicking Leigh syndrome [27]. Treatment with fenofibrate (100 $mg \cdot kg^{-1} \cdot day^{-1}$, *i.p.*), which has favorable physicochemical properties (*e.g.* enhanced solubility) compared to other fibrates, extended the median survival from postnatal day (PD) 45 to PD 49, with the longest-lived mouse surviving 58 days (Fig. 4A).

Up to PD 35 no differences in bodyweight were observed (Fig. 4B). Fenofibrate significantly increased the ability of *Ndufs4*$^{-/-}$ mice to complete a walking session at higher ages (Fig. 4C). As muscle weakness and involuntary movements are among the most burdensome clinical symptoms in CI-deficient patients [40], we examined motor function in more detail. Fenofibrate did not restore the increased run duration or decreased paw pressure in *Ndufs4*$^{-/-}$ mice (Fig. 4D–E). Next, we investigated the various types of gait support (Fig. 4F). Wildtype and *Ndufs4*$^{-/-}$ mice mainly rely on diagonal support, which is impaired in *Ndufs4*$^{-/-}$ mice and not corrected by fenofibrate (Fig. 4F–G). Increased support on either hind or front paws (*i.e.* girdle support) was restored (Fig. 4H), but fenofibrate could not correct the reliance on single, lateral,

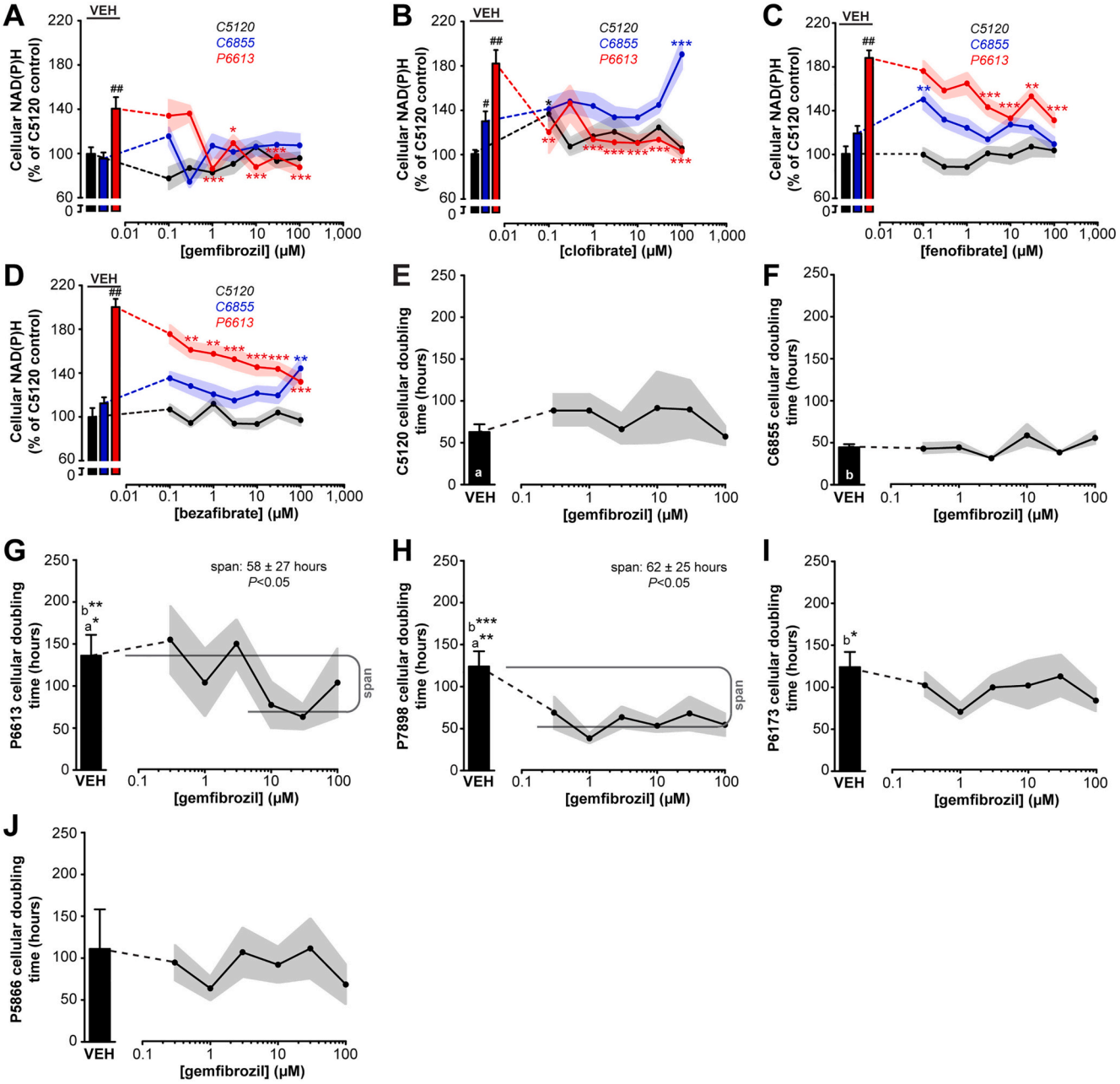

Fig. 3. Fibrates dose-dependently decrease cellular NAD(P)H levels and attenuate cell growth defects in CI-deficient fibroblasts. Dose-dependent effects of (A) gemfibrozil, (B) clofibrate, (C) fenofibrate, or (D) bezafibrate treatment on NAD(P)H levels after incubation for 24 h in control and patient fibroblasts (normalized to C5120 vehicle (VEH) (55 ± 3 AU), n ≥ 21 cells in each experiment (n = 3)). (E–J) Cellular doubling times of gemfibrozil-treated fibroblasts of (E–F) controls and CI-deficient patients (G) P6613, (H) P7898, (I) P6173, and (J) P5866. Grey lines indicate the dose-response curve top and bottom. Data are presented as means ± SEM. (A–D) $^{\#\#}p < 0.01$ compared to C5120 control levels or $^{*}p < 0.05$; $^{**}p < 0.01$; $^{***}p < 0.001$ to evaluate treatment effects, by one-way ANOVA with Dunnett's *post hoc* analysis. (E–J) a,b$^{*}p < 0.05$; a,b$^{**}p < 0.01$, a,b$^{***}p < 0.001$; (G–J) compared to control (a:C5120, b:C6855) VEH levels, by one-way ANOVA with Dunnett's *post hoc* analysis. Span (G–H) was tested to be significantly non-zero.

three or four paw support (Fig. 4I–L). This suggests that the increased overall walking ability is not due to an increased coordination or paw pressure, but other gait determinants not investigated in this study.

In vivo cellular effects of fibrate treatment were investigated by measuring cholesterol efflux rates in freshly isolated peritoneal macrophages (Fig. 4M–N). Total unsupported cholesterol efflux (*i.e.* without cholesterol acceptor proteins) was increased in untreated *Ndufs4*$^{-/-}$ mice, in line with a compensatory role of this pathway in CI deficiency, and was, as in wildtype mice, further increased by fenofibrate (Fig. 4M). Moreover, fenofibrate increased apoA-I-supported cholesterol efflux in these cells (Fig. 4N). This is indicative for the involvement of ABCA1, in accordance with our findings in CI-deficient patient fibroblasts (Fig. 2E–G). Fenofibrate did also elevate plasma cholesterol levels in both wildtype and *Ndufs4*$^{-/-}$ mice (Fig. 4O), which can be explained by an increased efflux of cholesterol into the systemic circulation. In line with our model predictions, bile cholesterol content was increased in untreated *Ndufs4*$^{-/-}$ mice (Fig. 4P), which is indicative of an increased systematic cholesterol efflux (*i.e.* reverse cholesterol transport, RCT). However, bile cholesterol levels were not further increased in fenofibrate-treated *Ndufs4*$^{-/-}$ mice, whereas they were increased in wildtype mice after fenofibrate treatment (Fig. 4P). This may potentially be explained by saturation of biliary cholesterol efflux [41,42], which

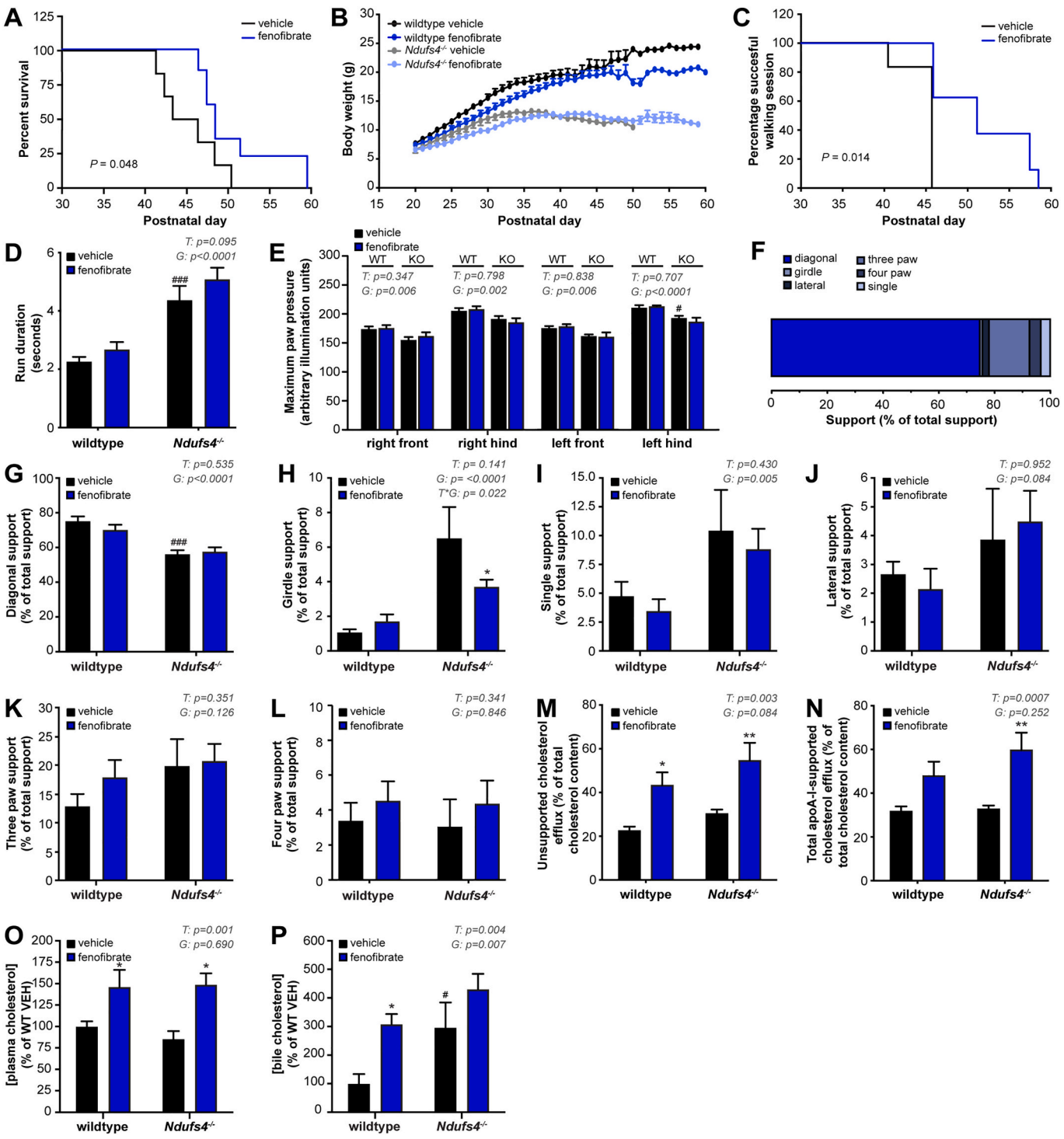

Fig. 4. Fibrate treatment improves life span and motor function in *Ndufs4*$^{-/-}$ mice accompanied by stimulation of cholesterol efflux. (**A**) Survival curves and of *Ndufs4*$^{-/-}$ mice treated intraperitoneally with 100 mg·kg bodyweight^{-1}·day^{-1} fenofibrate (■) or vehicle control (■) from postnatal day (PD) 20 onwards. (**B**) Bodyweight was assessed in wildtype and *Ndufs4*$^{-/-}$ mice with or without fenofibrate treatment (see legend in panel for color coding). (**C–L**) Motor function analysis included (**C**) the percentage of mice that successfully completed a walking session, (**D**) run duration, and (**E**) paw pressure and (**F**) Wildtype vehicle composition of the various types of support. (**G–L**) Percentage of (**G**) diagonal, (**H**) girdle, (**I**) single, (**J**) lateral, (**K**) three paw, and (**L**) four paw support. (**M–N**) Cellular cholesterol efflux from peritoneal macrophages; (**M**) unsupported and (**N**) apoA-I-supported cholesterol efflux was determined and expressed as the percentage of all radioactively labelled control (*i.e.* present in both cellular and medium fraction). (**O**) Plasma and (**P**) bile cholesterol levels were normalized to wildtype vehicle control (plasma 1.9 ± 0.1 mM; bile 1.3 ± 0.3 mM). Data are presented as means ± SEM; n = 23 vehicle-treated animals (n = 13 wildtype, n = 10 *Ndufs4*$^{-/-}$) n = 16 fenofibrate-treated animals (n = 8 wildtype, n = 8 *Ndufs4*$^{-/-}$). (**A, C**) Survival plot differences were analyzed by Mantel-Cox tests. (**B**) Body weight was compared up to PD 35 using linear mixed model analysis (**D, E, G–O**) $^{\#}p < 0.05$, $^{\#\#\#}p < 0.001$ to compare genotype vehicle differences or $^{*}p < 0.05$, $^{**}p < 0.01$, to compare treatment effects, by two-way ANOVA (*G*: genotype; *T*: treatment; *T*G*: treatment*genotype interaction) with Bonferroni's *post hoc* analysis.

could already have taken place in *Ndufs4*$^{-/-}$ mice, but not wildtype, mice.

Previously observed beneficial effects of bezafibrate on mitochondrial disease pathology have been explained by PGC-1α-dependent upregulation of fatty-acid β-oxidation and increased mitochondrial mass [43–50]. In contrast, we observed no significant changes in fatty-acid-driven respiration were observed in control or CI-deficient fibroblasts, or in muscle fibers from wildtype or *Ndufs4*$^{-/-}$ mice (Supplementary Fig. A.4A–B). Moreover, gemfibrozil treatment did not result in detectable changes in mitochondrial mass in control or patient fibroblasts (Supplementary Fig. A.4C–D). These findings support that stimulation of cholesterol efflux and consequent acceleration of cholesterol biosynthesis is the most relevant beneficial effect of fibrates in CI-deficiency.

Finally, PGC-1α and PPARγ activation are likely related to the previously observed hepatotoxic effects of bezafibrate in mice [44,48]. Liver weight was increased with fenofibrate (Supplementary Fig. A.5A), accompanied by elevated plasma ALAT levels (Supplementary Fig. A.5B). However, fenofibrate did not detectably increase plasma ASAT levels or total hepatic lipid content (Supplementary Fig. A.5C–D). Upon histological examination, fenofibrate displayed some small focal lesions in wildtype and *Ndufs4*$^{-/-}$ mice (Supplementary Fig. A.5E), although more diffuse lesions were observed in *Ndufs4*$^{-/-}$ mice (Supplementary Fig. A.5F). Overall, hepatotoxicity by fenofibrate appeared to be mild as compared to the results described for bezafibrate, which may be attributed to its greater PPAR-α specificity.

4. Discussion

Using an integrative computational and experimental approach, we were able to identify cholesterol biosynthesis as an important component in compensating the impaired redox state due to CI-deficiency. The beneficial effects of fibrates in CI-deficient patient fibroblasts is in agreement with the previously observed favorable effects of bezafibrate in several mouse models of cytochrome *c* oxidase (COX) or CIV deficiency, as reviewed previously [44,49], and short-term beneficial effects recently observed after bezafibrate treatment of patients with mitochondrial myopathies [47]. Although bezafibrate was not beneficial in all mouse models, overexpression of PGC-1α increased COX activity and mitochondrial biogenesis in all cases. Apparently, PGC-1α is activated through PPAR in bezafibrate-sensitive models.

Additional studies using alternative models also explained the positive effects of PPAR-α stimulation by an increased PGC-1α expression, leading to increases in OXPHOS capacity, fatty acid oxidation and mitochondrial mass [44,46]. We could, however, not demonstrate an effect on any of these pathways, which argues against an involvement of the PPAR-PGC-1α pathway in CI-deficient patient fibroblast. This has led to the idea that the mode of action of fibrates could be beneficial for mitochondrial disease by stimulating multiple metabolic pathways, of which the cholesterol synthesis may be most relevant for CI-deficiency.

However, in none of these studies the effect on cholesterol biosynthesis or efflux was investigated. Our study is, to the best of our knowledge, the first to demonstrate that fenofibrate treatment of *Ndufs4*$^{-/-}$ CI-deficient mice induced an increased cellular cholesterol efflux. These effects could be associated with improved survival and motor function, which is in line with the beneficial effects of fibrates previously observed in mitochondrial disease models [45,46]. In addition, the improved motor function illustrates the clinical relevance of our results, as recent results have suggested that this is a valid outcome measure for patients with an OXPHOS deficiency [40,51].

The improved motor function could be associated with a reduced brain lesions characteristic for the disease phenotype, as also observed in a previous study where we investigated the effects of the ROS-redox modulator KH176 in *Ndufs4*$^{-/-}$ mice [31]. Combined with the notion that the *Ndufs4*$^{-/-}$ phenotype relies mainly on a declined CNS function, this warrants further investigation of the effects of fenofibrate on neuronal cholesterol efflux, NAD(P)H levels and characteristic brain lesions. Although fibrates have a limited brain permeability [53,54], we have previously demonstrated that clofibrate does reach pharmacologically relevant levels in the brain of *Ndufs4*$^{-/-}$ mice [55]. We therefore argued that the effects observed on cholesterol efflux in peritoneal macrophages and the absence of an effect on mitochondrial fatty acid oxidation in muscles will also translate to brain tissue.

The use of more potent NAD(P)H-lowering fibrates (*i.e.* gemfibrozil and clofibrate) may be associated with a more effective treatment of mitochondrial disease with a better balance between benefit and risk of liver injury. Clinical application of bezafibrate is expected to be limited because of its potent hepatotoxicity, which was previously observed in mice with late-onset mitochondrial myopathy [44]. We observed minor alterations in liver histology in fenofibrate-treated mice, and liver weight was increased 1.9-fold, as compared to a more than two-fold increase in previous studies showing overt liver hepatotoxicity upon bezafibrate treatment [44,48,49]. These effects could be due to the differences in PPAR-agonist potency, but are more likely explained by the high PPAR-α specificity of fenofibrate as compared to a pan-agonist (α, δ, γ) like bezafibrate [39].

We could also demonstrate a beneficial effect of fibrate treatment on the cellular growth rates of two out of four tested CI-deficient patient fibroblasts. These results are in line with the previously observed beneficial effects of lowered cellular NADH levels when mitochondrial function is decreased [7,8,9]. Remarkably, these two fibroblast cell lines (P6613 and P7898) were derived from the most short-lived patients studied (Supplementary Table A.1). This may suggest that these patients had not increased their cellular cholesterol efflux to adapt to the disease state, whereas this may have been the case in the longer-lived patients (P6173 and P5866).

The novel link between cholesterol synthesis and cellular redox state in CI-deficiency could also provide novel insights into the pathophysiological mechanisms of other diseases, like inborn errors of sterol metabolism, in which a decreased cholesterol synthesis could as well be expected to increase NAD(P)H levels [52]. *Via* the activity of NADPH oxidases this could lead to an increased ROS generation [10,11], eventually contributing to cellular damage and the observed disease phenotype. Further studies are, however, needed to determine whether NAD(P)H levels are indeed increased and whether these increased levels lead to increased cytosolic ROS generation by NADPH oxidases. Although a role of NADPH oxidase-dependent ROS generation has been described in mitochondrial dysfunction due to loss of COX [11], it needs to be verified whether this pathway is also key to the increased ROS levels in CI deficiency. In addition to inherited metabolic diseases, this link we identified between cholesterol synthesis and cellular redox state in CI deficiency may also be of relevance to common diseases, such as cancer. Cholesterol biosynthesis has demonstrated to promote tumorigenesis [56], a process which is also associated with increased ROS generation by NADPH oxidases [57]. It would therefore be worthwhile to study the putative relationship between cholesterol biosynthesis and ROS levels in cancer progression.

Our work could also explain part the short-term beneficial effects recently observed after bezafibrate treatment of patients with mitochondrial myopathies [47]. Moreover, PPAR-α-targeted stimulation of the cholesterol production and export may prevent long-term deregulation of mitochondrial fatty acid and amino acid metabolism as has been observed with an unspecific PPAR-agonist, like bezafibrate.

To conclude, we demonstrate the potential of the cholesterol biosynthesis pathway to compensate for a disturbed cellular redox state in CI-deficiency. Additional pharmacological activation of this pathway normalized the cellular redox state and increased the lifespan and motor function of CI-deficient mice. Our results indicate the presence of compensatory biological pathways in mitochondrial dysfunction, thereby providing a framework to explore novel therapeutic interventions for mitochondrial diseases for which currently no cure exists.

Supplementary data to this article can be found online at https://doi.

org/10.1016/j.bbadis.2020.166062.

Funding

This research was supported by a grant from the Netherlands Organization for Scientific Research NWO Centers for Systems Biology Research initiative to JS (CSBR09/013V), a Prinses Beatrix Spierfonds research grant (W.OR16-19) and a grant from the Radboud University Medical Center (RIMLS 017-010a).

CRediT authorship contribution statement

Tom J.J. Schirris: Conceptualization, Investigation, Formal analysis, Writing – original draft, Writing – review & editing. **Sergio Rossell:** Conceptualization, Investigation, Formal analysis, Writing – original draft, Writing – review & editing. **Ria de Haas:** Conceptualization, Investigation, Formal analysis, Writing – review & editing. **Sanne J.C. M. Frambach:** Investigation, Formal analysis, Writing – review & editing. **Charlotte A. Hoogstraten:** Investigation, Formal analysis, Writing – review & editing. **G. Herma Renkema:** Investigation, Formal analysis, Writing – review & editing. **Julien D. Beyrath:** Investigation, Formal analysis, Writing – review & editing. **Peter H.G.M. Willems:** Conceptualization, Investigation, Formal analysis, Writing – original draft, Writing – review & editing. **Martijn A. Huynen:** Conceptualization, Writing – review & editing, Funding acquisition. **Jan A.M. Smeitink:** Conceptualization, Writing – review & editing, Funding acquisition. **Frans G.M. Russel:** Conceptualization, Writing – review & editing, Funding acquisition. **Richard A. Notebaart:** Conceptualization, Writing – review & editing, Funding acquisition.

Declaration of competing interest

JS, GR, and JB hold (partial) positions at Khondrion BV, a Radboud University Medical Center spin-out company founded by JS.

References

[1] L. Galluzzi, O. Kepp, M.G. Vander Heiden, G. Kroemer, Metabolic targets for cancer therapy, Nat. Rev. Drug Discov. 12 (2013) 829–846, https://doi.org/10.1038/nrd4145.
[2] A. Johri, N.Y. Calingasan, T.M. Hennessey, A. Sharma, L. Yang, E. Wille, A. Chandra, M.F. Beal, Pharmacologic activation of mitochondrial biogenesis exerts widespread beneficial effects in a transgenic mouse model of Huntington's disease, Hum. Mol. Genet. 21 (2012) 1124–1137, https://doi.org/10.1093/hmg/ddr541.
[3] W.J. Koopman, P.H. Willems, J.A. Smeitink, Monogenic mitochondrial disorders, N. Engl. J. Med. 366 (2012) 1132–1141, https://doi.org/10.1056/NEJMra1012478.
[4] A.M. Walters, G.A. Porter Jr., P.S. Brookes, Mitochondria as a drug target in ischemic heart disease and cardiomyopathy, Circ. Res. 111 (2012) 1222–1236, https://doi.org/10.1161/CIRCRESAHA.112.265660.
[5] S. Rahman, D.R. Thorburn, 189th ENMC international workshop complex I deficiency: diagnosis and treatment 20–22 April 2012, Naarden, The Netherlands, Neuromuscul. Disord. 23 (2013) 506–515, https://doi.org/10.1016/j.nmd.2013.03.004.
[6] F. Distelmaier, W.J. Koopman, L.P. van den Heuvel, R.J. Rodenburg, E. Mayatepek, P.H. Willems, J.A. Smeitink, Mitochondrial complex I deficiency: from organelle dysfunction to clinical disease, Brain. 132 (2009) 833–842, https://doi.org/10.1093/brain/awp058.
[7] D.V. Titov, V. Cracan, R.P. Goodman, J. Peng, Z. Grabarek, V.K. Mootha, Complementation of mitochondrial electron transport chain by manipulation of the NAD+/NADH ratio, Science. 352 (2016) 231–235, https://doi.org/10.1126/science.aad4017.
[8] V. Cracan, D.V. Titov, H. Shen, Z. Grabarek, V.K. Mootha, A genetically encoded tool for manipulation of NADP(+)/NADPH in living cells, Nat. Chem. Biol. 13 (2017) 1088–1095, https://doi.org/10.1038/nchembio.2454.
[9] A. Patgiri, O.S. Skinner, Y. Miyazaki, G. Schleifer, E. Marutani, H. Shah, R. Sharma, R.P. Goodman, T.L. To, X. Robert Bao, F. Ichinose, W.M. Zapol, V.K. Mootha, An engineered enzyme that targets circulating lactate to alleviate intracellular NADH: NAD+ imbalance, Nat. Biotechnol. 38 (2020) (2020) 309–313, https://doi.org/10.1038/s41587-019-0377-7.
[10] Y.-S. Kim, M.J. Morgan, S. Choksi, Z.-G. Liu, TNF-induced activation of the Nox1 NADPH oxidase and its role in the induction of necrotic cell death, Mol. Cell 26 (2007) 675–687, https://doi.org/10.1016/j.molcel.2007.04.021.
[11] J.E. Leadsham, G. Sanders, S. Giannaki, E.L. Bastow, R. Hutton, W.R. Naeimi, M. Breitenbach, C.W. Gourlay, Loss of cytochrome c oxidase promotes RAS-dependent ROS production from the ER resident NADPH oxidase, Yno1p, in yeast, Cell Metab. 18 (2013) 279–286, https://doi.org/10.1016/j.cmet.2013.07.005.
[12] S. Verkaart, W.J. Koopman, J. Cheek, S.E. van Emst-de Vries, L.W. van den Heuvel, J.A. Smeitink, P.H. Willems, Mitochondrial and cytosolic thiol redox state are not detectably altered in isolated human NADH:ubiquinone oxidoreductase deficiency, Biochim. Biophys. Acta 1772 (2007) 1041–1051, https://doi.org/10.1016/j.bbadis.2007.05.004.
[13] F. Valsecchi, C. Monge, M. Forkink, A.J.C. de Groof, G. Benard, R. Rossignol, H. G. Swarts, S.E. van Emst-de Vries, R.J. Rodenburg, M.A. Calvaruso, L.G. J. Nijtmans, B. Heeman, P. Roestenberg, B. Wieringa, J.A.M. Smeitink, W.J. H. Koopman, P.H.G.M. Willems, Metabolic consequences of NDUFS4 gene deletion in immortalized mouse embryonic fibroblasts, Biochim. Biophys. Acta Bioenerg. 1817 (2012) 1925–1936, https://doi.org/10.1016/j.bbabio.2012.03.006.
[14] S. Schwörer, M. Berisa, S. Violante, W. Qin, J. Zhu, R.C. Hendrickson, J.R. Cross, C. B. Thompson, Proline biosynthesis is a vent for TGFβ-induced mitochondrial redox stress, EMBO J. (2020) 1–20, https://doi.org/10.15252/embj.2019103334.
[15] N.C. Duarte, S.A. Becker, N. Jamshidi, I. Thiele, M.L. Mo, T.D. Vo, R. Srivas, B. O. Palsson, Global reconstruction of the human metabolic network based on genomic and bibliomic data, Proc. Natl. Acad. Sci. U. S. A. 104 (2007) 1777–1782, https://doi.org/10.1073/pnas.0610772104.
[16] S.M. Kelk, B.G. Olivier, L. Stougie, F.J. Bruggeman, Optimal flux spaces of genome-scale stoichiometric models are determined by a few subnetworks, Sci. Rep. 2 (2012) 580, https://doi.org/10.1038/srep00580.
[17] S. Rossell, M.A. Huynen, R.A. Notebaart, Inferring metabolic states in uncharacterized environments using gene-expression measurements, PLoS Comput. Biol. 9 (2013), e1002988, https://doi.org/10.1371/journal.pcbi.1002988.
[18] R. Mahadevan, C.H. Schilling, The effects of alternate optimal solutions in constraint-based genome-scale metabolic models, Metab. Eng. 5 (2003) 264–276. http://www.ncbi.nlm.nih.gov/pubmed/14642354.
[19] A.M. Voets, M. Huigsloot, P.J. Lindsey, A.M. Leenders, W.J. Koopman, P. H. Willems, R.J. Rodenburg, J.A. Smeitink, H.J. Smeets, Transcriptional changes in OXPHOS complex I deficiency are related to anti-oxidant pathways and could explain the disturbed calcium homeostasis, Biochim. Biophys. Acta 1822 (2012) 1161–1168, https://doi.org/10.1016/j.bbadis.2011.10.009.
[20] P. Costet, F. Lalanne, M.C. Gerbod-Giannone, J.R. Molina, X. Fu, E.G. Lund, L. J. Gudas, A.R. Tall, Retinoic acid receptor-mediated induction of ABCA1 in macrophages, Mol. Cell. Biol. 23 (2003) 7756–7766. http://www.ncbi.nlm.nih.gov/pubmed/14560020.
[21] S. Montero-Villegas, M. Polo, M. Galle, B. Rodenak-Kladniew, M. Castro, A. Ves-Losada, R. Crespo, M. Garcia de Bravo, Inhibition of mevalonate pathway and synthesis of the storage lipids in human liver-derived and non-liver cell lines by Lippia alba essential oils, Lipids. 52 (2017) 37–49, https://doi.org/10.1007/s11745-016-4218-x.
[22] H. Niu, Y. Chao, K. Li, J. Li, W. Gong, W. Huang, Robinetinidol-flavone attenuates cholesterol synthesis in hepatoma cells via inhibition of 3-hydroxy-3-methylglutaryl-coenzyme A reductase, Mol. Med. Rep. 11 (2015) 561–566, https://doi.org/10.3892/mmr.2014.2758.
[23] A.V. Kuznetsov, V. Veksler, F.N. Gellerich, V. Saks, R. Margreiter, W.S. Kunz, Analysis of mitochondrial function in situ in permeabilized muscle fibers, tissues and cells, Nat. Protoc. 3 (2008) 965–976, https://doi.org/10.1038/nprot.2008.61.
[24] T.J. Schirris, G.H. Renkema, T. Ritschel, N.C. Voermans, A. Bilos, B.G. van Engelen, U. Brandt, W.J. Koopman, J.D. Beyrath, R.J. Rodenburg, P.H. Willems, J. A. Smeitink, F.G. Russel, Statin-induced myopathy is associated with mitochondrial complex III inhibition, Cell Metab. 22 (2015) 399–407, https://doi.org/10.1016/j.cmet.2015.08.002.
[25] M. Forkink, F. Basit, J. Teixeira, H. Swarts, W.J.H. Koopman, P.H.G.M. Willems, Complex I and complex III inhibition specifically increase cytosolic hydrogen peroxide levels without inducing oxidative stress in HEK293 cells, Redox Biol. 6 (2015) 607–616, https://doi.org/10.1016/j.redox.2015.09.003.
[26] R.J. Rodenburg, Biochemical diagnosis of mitochondrial disorders, J. Inherit. Metab. Dis. 34 (2011) 283–292, https://doi.org/10.1007/s10545-010-9081-y.
[27] F. Distelmaier, W.J.H. Koopman, E.R. Testa, A.S. de Jong, H.G. Swarts, E. Mayatepek, J.A.M. Smeitink, P.H.G.M. Willems, Life cell quantification of mitochondrial membrane potential at the single organelle level, Cytometry A 73 (2008) 129–138, https://doi.org/10.1002/cyto.a.20503.
[28] A.E. Carpenter, T.R. Jones, M.R. Lamprecht, C. Clarke, I.H. Kang, O. Friman, D. A. Guertin, J.H. Chang, R.A. Lindquist, J. Moffat, P. Golland, D.M. Sabatini, CellProfiler: image analysis software for identifying and quantifying cell phenotypes, Genome Biol. 7 (2006) R100, https://doi.org/10.1186/gb-2006-7-10-r100.
[29] S.E. Kruse, W.C. Watt, D.J. Marcinek, R.P. Kapur, K.A. Schenkman, R.D. Palmiter, Mice with mitochondrial complex I deficiency develop a fatal encephalomyopathy, Cell Metab. 7 (2008) 312–320, https://doi.org/10.1016/j.cmet.2008.02.004.
[30] A. Quintana, S.E. Kruse, R.P. Kapur, E. Sanz, R.D. Palmiter, Complex I deficiency due to loss of Ndufs4 in the brain results in progressive encephalopathy resembling Leigh syndrome, Proc. Natl. Acad. Sci. U. S. A. 107 (2010) 10996–11001, https://doi.org/10.1073/pnas.1006214107.
[31] R. de Haas, D. Das, A. Garanto, H.G. Renkema, R. Greupink, P. van den Broek, J. Pertijs, R.W.J. Collin, P. Willems, J. Beyrath, A. Heerschap, F.G. Russel, J. A. Smeitink, Therapeutic effects of the mitochondrial ROS-redox modulator KH176 in a mammalian model of Leigh Disease, Sci. Rep. 7 (2017) 11733, https://doi.org/10.1038/s41598-017-09417-5.

[32] S.C. Johnson, M.E. Yanos, E.-B. Kayser, A. Quintana, M. Sangesland, A. Castanza, L. Uhde, J. Hui, V.Z. Wall, A. Gagnidze, K. Oh, B.M. Wasko, F.J. Ramos, R. D. Palmiter, P.S. Rabinovitch, P.G. Morgan, M.M. Sedensky, M. Kaeberlein, mTOR inhibition alleviates mitochondrial disease in a mouse model of Leigh syndrome, Science (80-.) 342 (2013) 1524–1528, https://doi.org/10.1126/science.1244360.

[33] G. Schumann, R. Bonora, F. Ceriotti, G. Ferard, C.A. Ferrero, P.F. Franck, F.J. Gella, W. Hoelzel, P.J. Jorgensen, T. Kanno, A. Kessner, R. Klauke, N. Kristiansen, J. M. Lessinger, T.P. Linsinger, H. Misaki, M. Panteghini, J. Pauwels, F. Schiele, H. G. Schimmel, G. Weidemann, L. Siekmann, C. International Federation of Clinical, M. Laboratory, IFCC primary reference procedures for the measurement of catalytic activity concentrations of enzymes at 37 degrees C. International Federation of Clinical Chemistry and Laboratory Medicine. Part 4. Reference procedure for the measurement of catalytic con, Clin. Chem. Lab. Med. 40 (2002) 718–724, https://doi.org/10.1515/CCLM.2002.124.

[34] Y.S. Cheng, Y. Zheng, J.S. VanderGheynst, Rapid quantitative analysis of lipids using a colorimetric method in a microplate format, Lipids. 46 (2011) 95–103, https://doi.org/10.1007/s11745-010-3494-0.

[35] P.M. Schaefer, S. Kalinina, A. Rueck, C.A. von Arnim, B. von Einem, NADH autofluorescence—a marker on its way to boost bioenergetic research, Cytometry A 95 (2019) 34–46.

[36] N.D. McKay, B. Robinson, R. Brodie, N. Rooke-Allen, Glucose transport and metabolism in cultured human skin fibroblasts, Biochim. Biophys. Acta, Mol. Cell Res. 762 (1983) 198–204.

[37] G. Chinetti, S. Lestavel, V. Bocher, A.T. Remaley, B. Neve, I.P. Torra, E. Teissier, A. Minnich, M. Jaye, N. Duverger, H.B. Brewer, J.C. Fruchart, V. Clavey, B. Staels, PPAR-alpha and PPAR-gamma activators induce cholesterol removal from human macrophage foam cells through stimulation of the ABCA1 pathway, Nat. Med. 7 (2001) 53–58, https://doi.org/10.1038/83348.

[38] C.L. Bisgaier, D.C. Oniciu, R.A.K. Srivastava, Comparative evaluation of gemcabene and PPAR ligands in transcriptional assays of peroxisome proliferator-activated receptors: implication for the treatment of hyperlipidemia and cardiovascular disease, J. Cardiovasc. Pharmacol. 72 (2018) 3–10.

[39] N.S. Ghonem, D.N. Assis, J.L. Boyer, Fibrates and cholestasis, Hepatology. 62 (2015) 635–643, https://doi.org/10.1002/hep.27744.

[40] S. Koene, S.B. Wortmann, M.C. de Vries, A.I. Jonckheere, E. Morava, I.J.M. de Groot, J.A.M. Smeitink, Developing outcome measures for pediatric mitochondrial disorders: which complaints and limitations are most burdensome to patients and their parents? Mitochondrion. 13 (2013) 15–24, https://doi.org/10.1016/j.mito.2012.11.002.

[41] R.P.J. Oude Elferink, A. Groen, Mechanisms of biliary lipid secretion and their role in lipid homeostasis, in: Semin. Liver Dis., 2000, pp. 293–306. Copyright© 2000 by Thieme Medical Publishers, Inc., 333 Seventh Avenue, New York.

[42] C.I. Wagner, B.W. Trotman, R.D. Soloway, Kinetic analysis of biliary lipid excretion in man and dog, J. Clin. Invest. 57 (1976) 473–477, https://doi.org/10.1172/JCI108299.

[43] J. Bastin, F. Aubey, A. Rotig, A. Munnich, F. Djouadi, Activation of peroxisome proliferator-activated receptor pathway stimulates the mitochondrial respiratory chain and can correct deficiencies in patients' cells lacking its components, J. Clin. Endocrinol. Metab. 93 (2008) 1433–1441, https://doi.org/10.1210/jc.2007-1701.

[44] C. Viscomi, E. Bottani, G. Civiletto, R. Cerutti, M. Moggio, G. Fagiolari, E.A. Schon, C. Lamperti, M. Zeviani, In vivo correction of COX deficiency by activation of the AMPK/PGC-1alpha axis, Cell Metab. 14 (2011) 80–90, https://doi.org/10.1016/j.cmet.2011.04.011.

[45] S. Srivastava, F. Diaz, L. Iommarini, K. Aure, A. Lombes, C.T. Moraes, PGC-1alpha/beta induced expression partially compensates for respiratory chain defects in cells from patients with mitochondrial disorders, Hum. Mol. Genet. 18 (2009) 1805–1812, https://doi.org/10.1093/hmg/ddp093.

[46] S. Yatsuga, A. Suomalainen, Effect of bezafibrate treatment on late-onset mitochondrial myopathy in mice, Hum. Mol. Genet. 21 (2012) 526–535, https://doi.org/10.1093/hmg/ddr482.

[47] H. Steele, A. Gomez-duran, A. Pyle, S. Hopton, J. Newman, R.J. Stefanetti, S. J. Charman, J.D. Parikh, L. He, C. Viscomi, D.G. Jakovljevic, K.G. Hollingsworth, A. J. Robinson, R.W. Taylor, L. Bottolo, R. Horvath, P.F. Chinnery, Metabolic effects of bezafibrate in mitochondrial disease 12 (2020), e11589, https://doi.org/10.15252/emmm.201911589.

[48] N. Rotllan, G. Llaverías, J. Julve, M. Jauhiainen, L. Calpe-Berdiel, C. Hernández, R. Simó, F. Blanco–Vaca, J.C. Escolà-Gil, Differential effects of gemfibrozil and fenofibrate on reverse cholesterol transport from macrophages to feces in vivo, Biochim. Biophys. Acta Mol. Cell Biol. Lipids 1811 (2011) 104–110, https://doi.org/10.1016/j.bbalip.2010.11.006.

[49] M. Kanabus, S.J. Heales, S. Rahman, Development of pharmacological strategies for mitochondrial disorders, Br. J. Pharmacol. 171 (2014) 1798–1817, https://doi.org/10.1111/bph.12456.

[50] G. Haemmerle, T. Moustafa, G. Woelkart, S. Buttner, A. Schmidt, T. van de Weijer, M. Hesselink, D. Jaeger, P.C. Kienesberger, K. Zierler, R. Schreiber, T. Eichmann, D. Kolb, P. Kotzbeck, M. Schweiger, M. Kumari, S. Eder, G. Schoiswohl, N. Wongsiriroj, N.M. Pollak, F.P. Radner, K. Preiss-Landl, T. Kolbe, T. Rulicke, B. Pieske, M. Trauner, A. Lass, R. Zimmermann, G. Hoefler, S. Cinti, E.E. Kershaw, P. Schrauwen, F. Madeo, B. Mayer, R. Zechner, ATGL-mediated fat catabolism regulates cardiac mitochondrial function via PPAR-alpha and PGC-1, Nat. Med. 17 (2011) 1076–1085, https://doi.org/10.1038/nm.2439.

[51] I. Dirks, S. Koene, R. Verbruggen, J.A. Smeitink, M. Jansen, I.J. Groot, Assisted 6-minute cycling test: an exploratory study in children, Muscle Nerve 54 (2016) 232–238, https://doi.org/10.1002/mus.25021.

[52] G.E. Herman, L. Kratz, Disorders of sterol synthesis: beyond Smith-Lemli-Opitz syndrome, Am. J. Med. Genet. C Semin. Med. Genet. 160C (2012) 301–321, https://doi.org/10.1002/ajmg.c.31340.

[53] D. Deplanque, P. Gelé, O. Pétrault, I. Six, C. Furman, M. Bouly, S. Nion, B. Dupuis, D. Leys, J.C. Fruchart, R. Cecchelli, B. Staels, P. Duriez, R. Bordet, Peroxisome proliferator-activated receptor-alpha activation as a mechanism of preventive neuroprotection induced by chronic fenofibrate treatment, J. Neurosci. 23 (2003) 6264–6271, https://doi.org/10.1523/JNEUROSCI.23-15-06264.2003.

[54] M. Grabacka, P. Waligorski, A. Zapata, D.A. Blake, D. Wyczechowska, A. Wilk, M. Rutkowska, H. Vashistha, R. Ayyala, T. Ponnusamy, V.T. John, F. Culicchia, A. Wisniewska-Becker, K. Reiss, Fenofibrate subcellular distribution as a rationale for the intracranial delivery through biodegradable carrier, J. Physiol. Pharmacol. 66 (2015) 233–247.

[55] S.J.C.M. Frambach, M.A.E. van de Wal, P.H.H. van den Broek, J.A.M. Smeitink, F. G.M. Russel, R. de Haas, T.J.J. Schirris, Effects of clofibrate and KH176 on life span and motor function in mitochondrial complex I-deficient mice, Biochim. Biophys. Acta Mol. basis Dis. 2020 (1866) 165727, https://doi.org/10.1016/j.bbadis.2020.16572.

[56] B. Huang, B. Liang Song, C. Xu, Cholesterol metabolism in cancer: mechanisms and therapeutic opportunities, Nat. Metab. 2 (2020) 132–141, https://doi.org/10.1038/s42255-020-0174-0.

[57] V. Sosa, T. Moliné, R. Somoza, R. Paciucci, H. Kondoh, M.E. LLeonart, Oxidative stress and cancer: an overview, Ageing Res. Rev. 12 (2013) 376–390, https://doi.org/10.1016/j.arr.2012.10.004.